PAPER

Check for updates

Controlling spatial structure in minimal microbial communities by sequential capillary assembly

Cameron Boggon, [iD][a] Jeremy P. H. Wong, [iD][ad] Arpita Sahoo, [iD][b]
Annelies S. Zinkernagel, [iD][c] Markus A. Seeger, [iD][b] Eleonora Secchi [iD] *[d] and Lucio Isa [iD] *[a]

Bacteria in surface-attached communities often engage in social interactions with neighbouring microbes. Spatial structure within these communities is thought to strongly influence these interactions, yet there is a significant lack of experimental platforms which allow for the tight spatial control of microbial interactions at the microscale, severely limiting our ability to investigate the relationship between spatial structure and community development. Here, we demonstrate a workflow for patterning and growing two bacterial species on a template with high throughput (~10^5 patterned cells per template) and micron-scale precision. We demonstrate a methodology for directional sequential capillary assembly of colloidal particles in combination with nanobody-functionalised particles that enable highly specific, bio-orthogonal binding reactions between bacteria and surface deposited particles. Using *Staphylococcus aureus* and *Escherichia coli* as model systems, we demonstrate how these organisms can be patterned in any desired spatial configuration where resulting communal growth can be monitored under the microscope. This technique enables careful investigations into the role of initial spatial structure on microbial interactions at low cell density, which is crucial to understanding and manipulating microbial community development.

Introduction

Bacteria are often found in dense, multispecies communities and social interactions between community members significantly dictate community function and composition.[1–5] Nutrient competition, toxin production and quorum sensing, in particular, have been implicated as strong mediators of these social interactions.[6–8] Yet, investigating these interactions *in vitro* remains challenging due to well-established limitations in culture-based approaches. For example, microbial communities that are batch-cultured in liquid media are often unstable and rapidly devolve into monospecies cultures due to heterogeneous fitness of the different organisms in a given culture medium.[9–11] There is a need, therefore, for novel approaches to co-culture microbial communities *in vitro* to investigate social interactions among their constituents.

A significant body of ecological theory supports the idea that spatial structuring in microbial communities helps to mediate the interaction strength between organisms and thus promote community stability and diversity.[6,11,12] *In vivo* imaging (using Fluorescence *In situ* Hybridisation based techniques) of bacterial communities taken from diverse environments, *e.g.* including the human mouth, skin, chronic wound infections, cystic fibrosis sputum and soil, further indicate that spatial structuring is widespread in microbial communities.[13–22] As a consequence, several *in vitro* platforms have been proposed for controlling the initial spatial organization of microbial communities and observing how the community develops. Firstly, droplet microfluidics has been used to compartmentalise batch liquid cultures into 'microchambers' that limit the distribution of metabolites and constrain the number of organisms interacting with each other.[23,24] Secondly, various microfluidic platforms that physically separate cells *via* a nutrient-permeable membrane, allowing for the study of cross-feeding between organisms, have been developed.[10,25,26] Third, 3D printing-based assays have been used to print microbial communities[27–29] and directly demonstrated that spatial structure can help protect susceptible bacteria from antagonistic compounds.[30,31]

While these methods have served to highlight the importance of spatial organisation in social interactions, it remains challenging to control spatial organisation at the microscopic length scales characteristic of most microbial interactions. Measurements of interaction distances in dense environments indicate that these length scales are on the order of 1–100 microns.[8,32,33] Assays used to probe

[a] Laboratory for Soft Materials and Interfaces, Department of Materials, ETH Zürich, Switzerland. E-mail: lucio.isa@mat.ethz.ch
[b] Institute of Medical Microbiology, University of Zurich, Switzerland
[c] Department of Infectious Diseases and Hospital Epidemiology, University Hospital Zurich, University of Zurich, Switzerland
[d] Institute of Environmental Engineering, Department of Civil, Environmental, and Geomatic Engineering, ETH Zürich, Switzerland. E-mail: secchi@ifu.baug.ethz.ch

interaction distance, however, have relied on randomly seeding organisms either in microfluidic chambers[34,35] or on agar,[36,37] thus offering little control in directly studying the role that initial spatial structure and interaction length-scales play in shaping community dynamics. Previously mentioned approaches for controlling spatial structure typically operate at the hundreds of microns to millimeter scale. For example, 3D printing, which is currently the only method for truly controlling the initial spatial structure of multiple organisms, generally involves printing droplets hundreds of microns in diameter thus far exceeding these length scales.[27,31]

In this work, we leverage a technique known as sequential Capillarity-Assisted Particle Assembly (sCAPA)[38–41] to enable the controlled design of spatial structure at micrometer scales. We pattern micron-sized colloidal particles *via* controlled evaporation of a particle suspension across an array of cavities (which we refer to as 'traps') on a substrate. These traps capture particles as the droplet's meniscus passes over them (described in detail in ref. 42). This procedure can be performed sequentially to obtain heterogeneous particle patterns on one template, either by depositing particles of the same size into the same trap[39,41] or differently sized particles into traps of different sizes.[43,44] The resulting pattern is entirely determined by the arrangement of traps on the template and the filling sequence.

We make two key developments to this procedure to allow for the patterning of different microbial species in a defined spatial structure. Firstly, we show that by functionalising particles with species-selective nanobodies, we can selectively bind bacteria to our particle-patterned template thus achieving any desired spatial configuration with near-single-cell precision. Secondly, we show that asymmetric, wedge-shaped traps can be used to selectively pattern different particles of the same size, thus keeping the 'nanobody patch size' for cell binding constant and potentially substantially increasing the number of different particles that can be patterned on one template.

To showcase this method, we demonstrate a protocol for patterning pairs of particles, in varying spatial structures, functionalised with three separate nanobodies, which target either *Staphylococcus aureus* or two strains of *Escherichia coli*. We outline how cells can be patterned, then placed in nutrient agar and cultured under the microscope, allowing measurements of statistically relevant distributions of lag-time, fraction of growing cells and growth rate. We believe this approach is a powerful tool for investigating the role of length scale and spatial structure in shaping microbial community interactions.

Results

Patterning colloidal particles in defined spatial structures

sCAPA allows for patterning hundreds of thousands of particles in defined locations with micron-scale precision. A droplet of particle suspension is placed in a polydimethylsiloxane (PDMS) microfluidic chip, whose bottom surface (referred to as the PDMS 'template') contains an array of traps, and the chip is left on a heated stage to allow the droplet to evaporate (Fig. 1, chip design illustrated in SI S1).[45,46] As the droplet evaporates, the meniscus recedes over the template, and there is an accumulation of particles at the meniscus edge. Then, as the meniscus passes over a trap in the template, the high density of particles at the droplet edge ensures a particle is captured in each trap and held there by capillary forces (Fig. 1a and b and SI S1). A detailed account of the mechanisms and design considerations underpinning sCAPA is outlined in ref. 42. In practice, very high deposition yields are achieved by carefully controlling the evaporation rate (by controlling the temperature of the heat stage), the trap depth and the receding contact angle of the droplet using small amounts of surfactant.

We utilise sCAPA to deposit particles functionalised with nanobodies, which capture and localise different bacteria in defined locations. Crucially, we use particles of the same size, but with different nanobody functionalisations, in order to keep a constant 'patch size' that the bacteria will bind to. Since conventional sCAPA is based on the size match between the traps and deposited particles, it cannot select where similarly-sized but differently-functionalised particles are deposited. To overcome this limitation, we developed an asymmetric, wedge-shaped trap design. We demonstrated that selective deposition of same-sized particles could be achieved exclusively by controlling the direction of deposition (Fig. 1a–d). When the deposition direction aligns with the slope of the trap, particles get trapped between the straight back wall of the wedge and the meniscus. In all other deposition directions, the particle does not encounter a back wall and thus does not get trapped but rolls out along with the receding meniscus. We can therefore control where particles are deposited by simply changing the orientation of the PDMS roof, which determines the deposition direction relative to the wedge orientation. This is easily achieved using double-sided sticky tape to stick the PDMS roof to the template, enabling easy removal and exchange of the roof (Fig. 1e).

To demonstrate the versatility of sCAPA using this wedge-shaped trap design and to quantify the deposition yields, we fabricated templates for depositing two particle types with varying spatial structures (Fig. 2a and b). We conjugated 2.7 μm streptavidin-functionalised particles with either Atto-488 (green) or Atto-550 (red) biotin to distinguish between deposited particles. In Fig. 2a, we demonstrate that spatial structure can be varied while maintaining a constant ratio of green to red particles, in this case 1:1, by altering the spatial autocorrelation. We quantify spatial correlation between red and green particles using the commonly employed metric of Moran's I (calculation detailed in SI S2). A value of $I = -1$ corresponds to a perfectly negatively correlated spatial structure, *i.e.* meaning that a red particle is surrounded only by green particles and *vice versa*, leading to a "sodium chloride crystal" pattern. Completely randomly distributed particles lead to a value of $I = 0$ and a value of $I > 0$ corresponds to a positive correlation, implying that particles
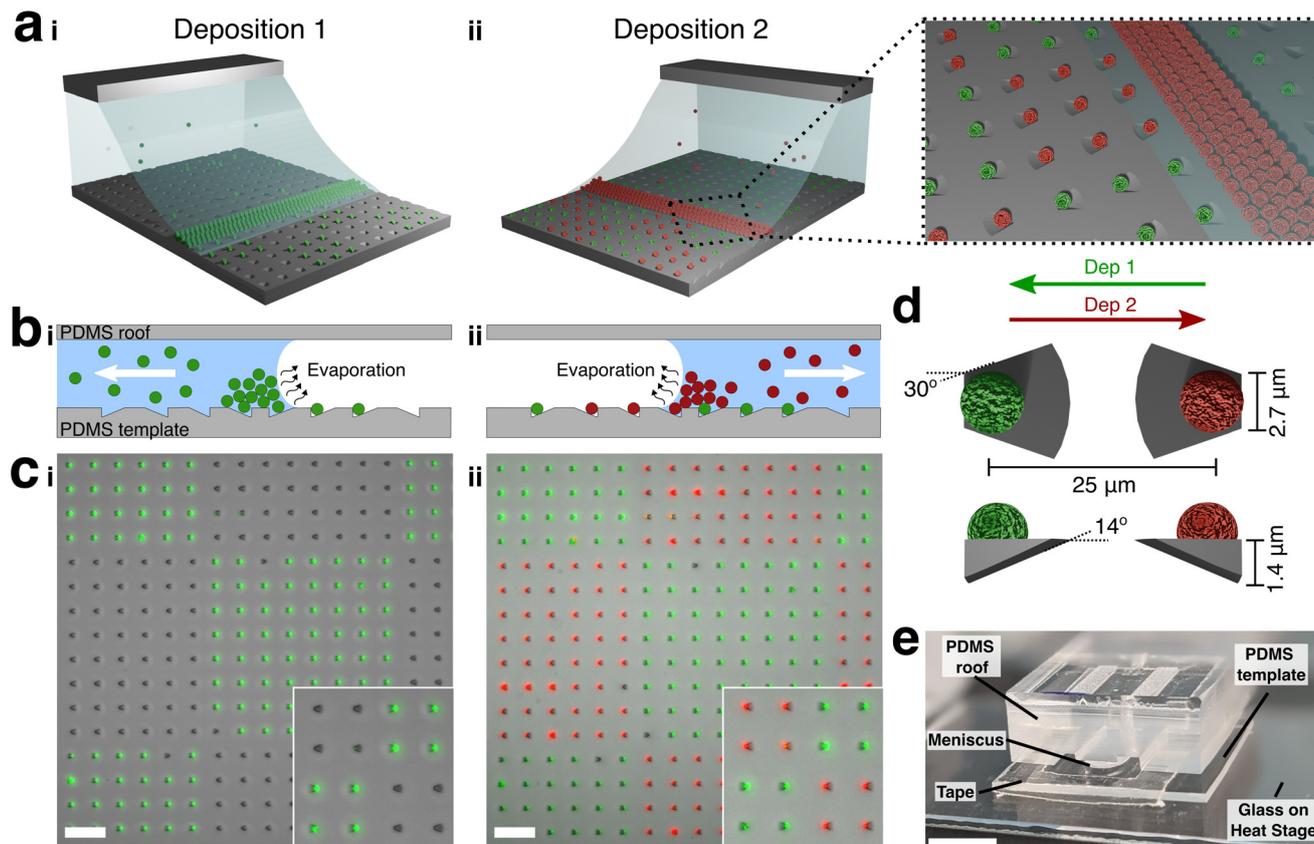
Fig. 1 Wedge-shaped traps enable directional sequential depositions of colloidal particles into targeted geometries. a) Graphical illustration of sequential deposition of colloidal particles into 3 × 3 square lattice traps. i) Deposition 1 with green particles. ii) Deposition 2, in the opposite direction, with red particles. b) Graphic of side-on view demonstrating deposition mechanism. As liquid in the channel evaporates (black wavy arrows), the meniscus moves backwards (white arrow marks direction of meniscus) and suspended particles accumulate in a dense zone at the meniscus edge. Particles are deposited only in traps where they encounter a back wall. i) Deposition 1 with green particles. ii) Deposition 2 in the opposite direction with red particles. c) Representative merged fluorescence and brightfield images after sequential depositions of 2.7 μm silica particles functionalised with Biotin-488 (green particles) or Biotin-550 (red particles). Inset: zoom-in images demonstrating specificity of deposited green or red particles into target traps. i) Template after deposition 1, ii) template after deposition 2. Scale bar = 50 μm. d) Graphical illustration of trap geometries used to capture single 2.7 μm silica particles. Arrows represent direction of moving meniscus used to deposit each particle colour. e) Labelled image of PDMS chip on a glass slide on a heat plate during deposition. Double-sided tape sticks PDMS roof to template, allowing easy exchange of roof to change deposition direction. Scale bar = 0.5 cm.

have similarly coloured neighbours. The template used in Fig. 2a iii is designed with 8 × 8 red/green alternating squares which corresponds to $I = 0.75$.

Spatial structure can also be modified by tuning the relative ratio of red and green particles. In Fig. 2b, we demonstrate control over the relative fraction of particles and their arrangements by designing arrays with a ratio of 1 : 24 red to green particles arranged in square lattices (i) and regular 1 : 8 ratio arrays with red particles surrounded by a circle of green particles (ii).

In order to achieve 2-particle depositions, we found a heating step between particle depositions to be critical in the procedure. Functionalising the silica particles with protein (either fluorescent-biotin or nanobodies) leads to weaker adhesion of the particles to the PDMS template after deposition, which leads to the particles deposited in the first deposition being removed upon the 2nd deposition. This was resolved by including a heating step of 1 minute between depositions (SI S3 for temperature screen). In order to

determine what temperature the particles actually 'experience' on the PDMS surface during this heat treatment, we measured the surface temperature using a thermistor. We found that when the heat plate was set to a nominal temperature of 130 °C, the measured surface temperature of the heat plate was 120 ± 1 °C and the surface of the PDMS template (~0.4 mm thick) was 87 ± 1 °C. While this heat step is usually not required for non-functionalised particles,[42] the necessity of such heat treatment has previously been reported for particles functionalised with DNA.[41] We think that a hydration layer is retained by the DNA/streptavidin–biotin functionalised layer at the particle surface, which reduces van der Waals adhesion, and which is evaporated by the heating step. Our findings suggest that a heating step of 87 ± 1 °C was sufficient to ensure reliable adhesion without noticeably damaging the biotin or the nanobodies, at least after 2 heating steps (see discussion below).

In Fig. 2c and d, we quantify deposition yields using standard particle localisation techniques on the brightfield,
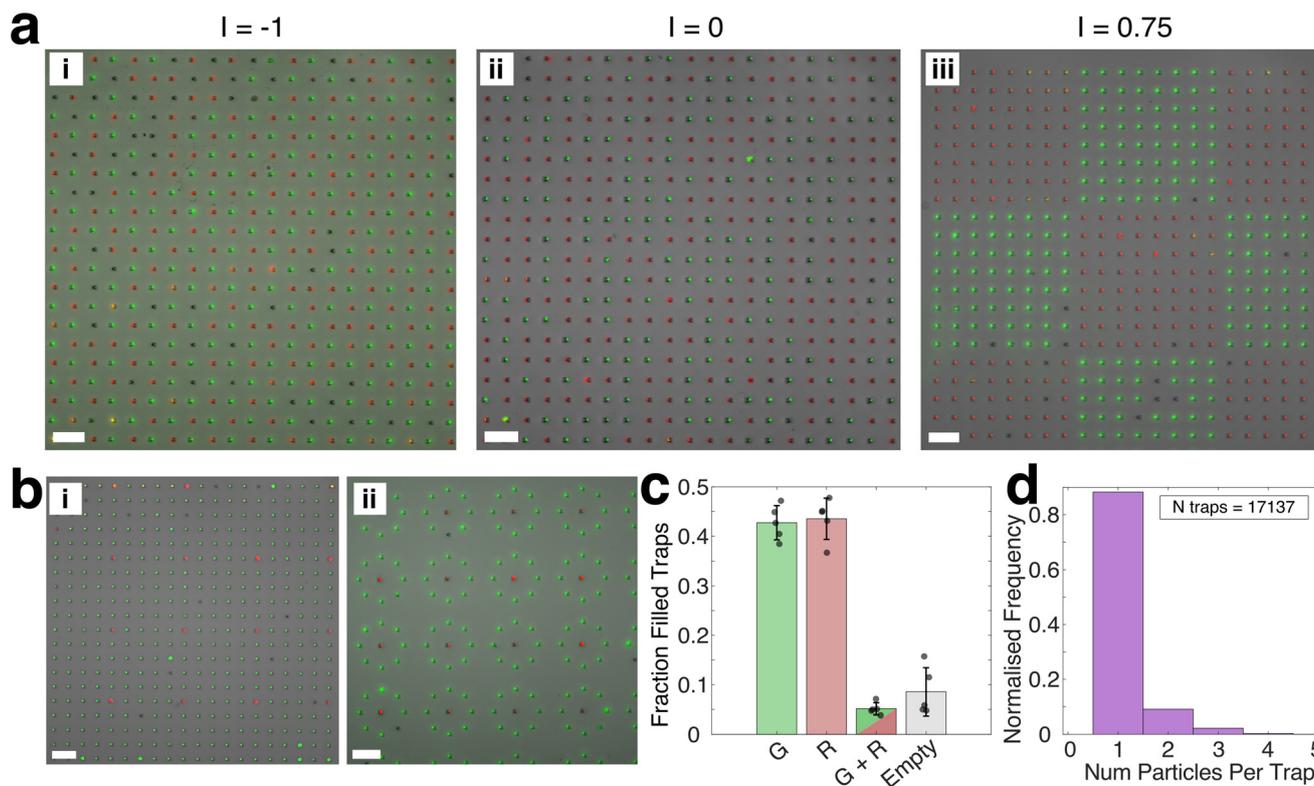
Fig. 2 Controlling spatial structure in two particle combinations. a) Varying spatial structure by autocorrelation using the Moran's I index (I). A 1:1 ratio of green and red particles are deposited in i) perfectly de-correlated "sodium chloride crystal" structure ($I = -1$), ii) unstructured, randomly distributed particles ($I = 0$), iii) patched square lattice of 8×8 red and green particles ($I = 0.75$). b) Varying spatial structure by relative fraction of red and green particles. i) 1:24 ratio of red to green particles in a square lattice. ii) 1:8 ratio of red to green particles in circular "corrals". All images in a and b are merged fluorescence and brightfield images. Scale bar = 50 μm. c) Quantification of the fractions of correctly and incorrectly deposited particles for templates in a (data combined for $I = -1$, $I = 0$ and $I = 0.75$). G = traps correctly filled by green particles, R = traps correctly filled by red particles, R + G = traps with both green and red particles (incorrect assembly), empty = traps with no particles. Bars and errors represent the average and standard error of the mean of 5 separate templates. Data points represent fractions for one template. d) Quantification of the number of particles found in each filled trap for data in a. The vast majority of traps are correctly filled with one particle.

green and red fluorescent channels after one deposition of each particle in each direction for the $I = -1$, $I = 0$ and $I = 0.75$ templates. In Fig. 2c, we measure the fraction of traps that were correctly filled, finding that an average of 86.3 ± 5.4% of traps are filled with the correctly coloured particle (cumulative average of 5 separate templates with 1:1 ratio of red and green particles). Incorrectly filled traps (traps containing one or more of the incorrect colour) and empty traps constituted 5.2 ± 1.2% and 8.6 ± 4.9%, respectively. In Fig. 2d, we quantify the number of particles per trap showing that a total of 88.3% contain only one particle per trap. Together, these data indicate that the wedge trap design is highly effective at selective, directional depositions and we can generate patterned particle configurations with high accuracy on micron length scales.

Selective binding of bacteria to target particles

Having determined that we can accurately assemble particles with defined spatial structures, we turned to engineering colloidal particles that bind microbes with high specificity. We leverage bio-orthogonal reactions targeting conserved proteins on the membrane of various bacteria. We focus on nanobodies due to their combination of high stability, strong binding affinity and their small size, which allows them to reach highly conserved proteins on the cell membrane that are often buried beneath long sugar molecules and therefore inaccessible to larger proteins like antibodies and lectins.[47,48]

We designed nanobody-functionalised particles by binding our streptavidin-functionalised particles *via* a biotin – PEG-11 – Maleimide linker to cysteine residues incorporated at the C-terminus of the nanobody (see graphic in Fig. 3a–c). Our nanobodies selectively bind to proteins on the membranes of *E. coli* or *S. aureus* (Fig. 3a–c). For *E. coli*, the nanobodies bind to two different isoforms of outer membrane protein A, which we denote as OmpA-short and OmpA-long.[48–51] We designed fluorescent strains that each express one of these two isoforms (see SI S12 for details). *E. coli* MC1061 natively producing OmpA-short is bound by Nb01 and *E. coli* ΔompA expressing OmpA-long from a plasmid is bound by Nb41 (*E. coli* strains hereafter referred to as *E. coli* (OmpA-short) and *E. coli* (OmpA-long), respectively). For *S. aureus*, we use synthetic nanobody F1 (SbF1), which binds to protein A, a highly abundant cell surface protein of *S. aureus*. Detailed
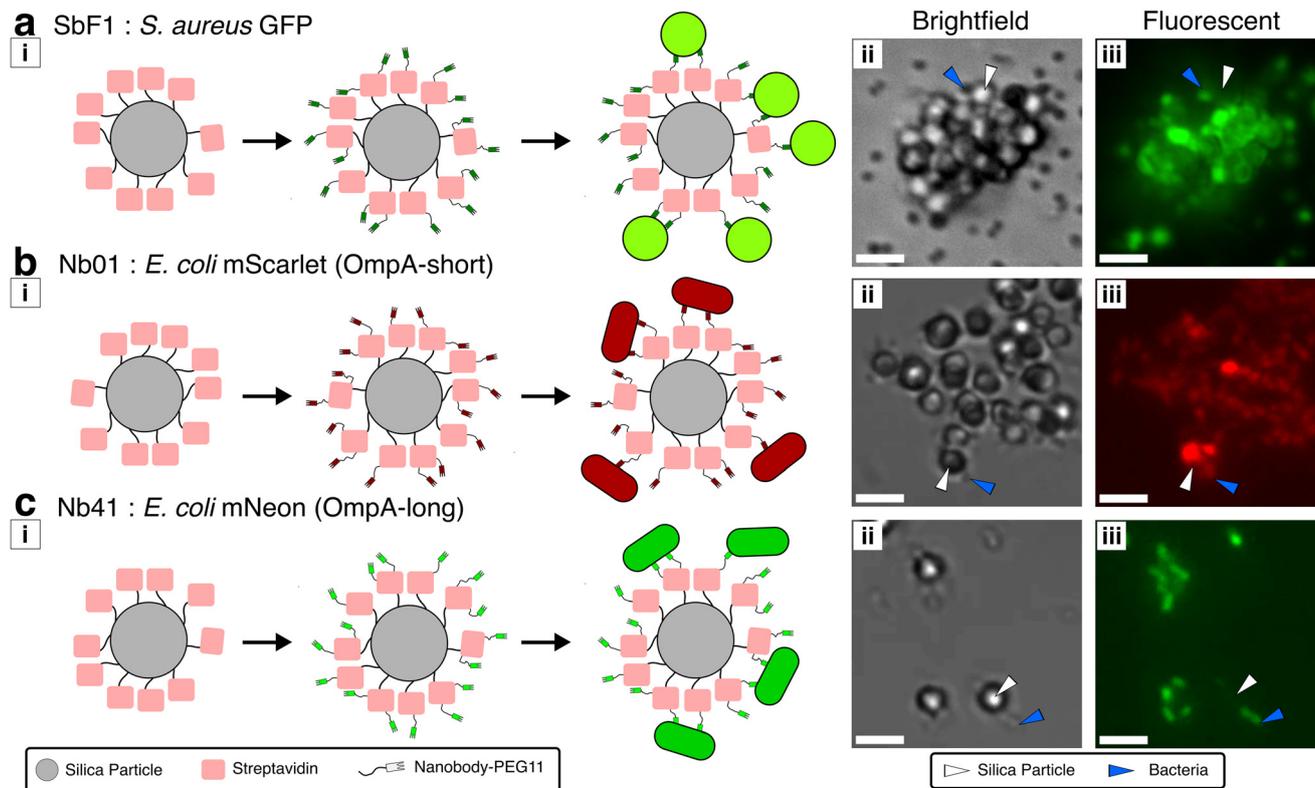
Fig. 3 Nanobody-functionalised silica particles bind selectively to target bacteria. i) Graphical illustration of particle–bacteria binding strategy. The cysteine group on the nanobody is bound to a PEG11 linker *via* a maleimide bond which, in turn, is bound to streptavidin-functionalised 2.7 μm silica particles *via* a biotin bond. ii) Particle–bacteria binding after mixing for 30 min in a 1.5 ml Eppendorf and imaging in a 96-well plate in the phase contrast channel or iii) fluorescence channel. White arrow highlights a silica particle, blue arrow highlights a bacterium. a) Sybody-F1 (SbF1) functionalised particles bound to *S. aureus* GFP. b) Nanobody 01 (Nb01) functionalised particles bound to *E. coli* MC1061 expressing mScarlet and naturally expressing OmpA-short. c) Nanobody 41 (Nb41) functionalised particles bound to *E. coli* MC1061 ΔompA expressing mNeonGreen and OmpA-long. Scale bar = 5 μm.

comments on the choice of target proteins and nanobodies are provided in SI S3. It should be noted, however, that protein A binds to the Fc-part of IgG-type antibodies as well as to a large proportion of nanobody scaffolds.[52,53] Indeed, we observed that Nb01, which is directed against OmpA-short, cross-reacts with protein A. Conversely, Nb41 directed against OmpA-long does not cross-react with protein A. As a consequence, we have two, strain-selective nanobody pairs: *S. aureus* and *E. coli* (OmpA-long), *E. coli* (OmpA-short) and *E. coli* (OmpA-long).

In Fig. 3, we demonstrate successful binding of the target organisms when nanobody-functionalised-particles and bacteria are mixed together in bulk liquid culture. We observe that *S. aureus* and *E. coli* (OmpA-short) bind tightly and with high specificity to SbF1 and Nb01, respectively, often leading to the assembly of large particle aggregates >50 μm in diameter (Fig. 3a and b).

We find that *E. coli* (OmpA-long), on the other hand, generally does not form aggregates (Fig. 3c), which likely reflects either a lower binding affinity or lower expression of OmpA-long on the cell surface. Nonetheless, single particles with robustly adhered bacterial cells can easily be observed. By combinatorial screening of all particles against

each bacterial strain, we confirmed the selectivity of our particle binding assay (Fig. 3a–c and SI S3). We therefore successfully engineered a colloidal system that binds bacteria with high specificity.

Targeted cell binding and growth after particle deposition with sCAPA

Having developed a selective particle binding strategy and a selective particle deposition strategy, we turn to establishing a growth protocol for long-term imaging of bacterial growth after particle deposition and cell binding on the sCAPA template.

Fig. 4 a summarised the protocol for binding and growth of one bacterial species (a more detailed graphical protocol is provided in SI S5). We first deposited nanobody-functionalised particles *via* sCAPA into target patterns. We then heat-treated the template, as above, before transferring it to a glass-bottomed Petri dish. It was crucial to ensure that the bacteria did not passively bind to the template and only bound to the target particles. We found that treating the template with bovine serum albumin (BSA) was very efficient passivating the PDMS surface without blocking access to the nanobodies. After exposure, we replaced the BSA with a washed bacterial
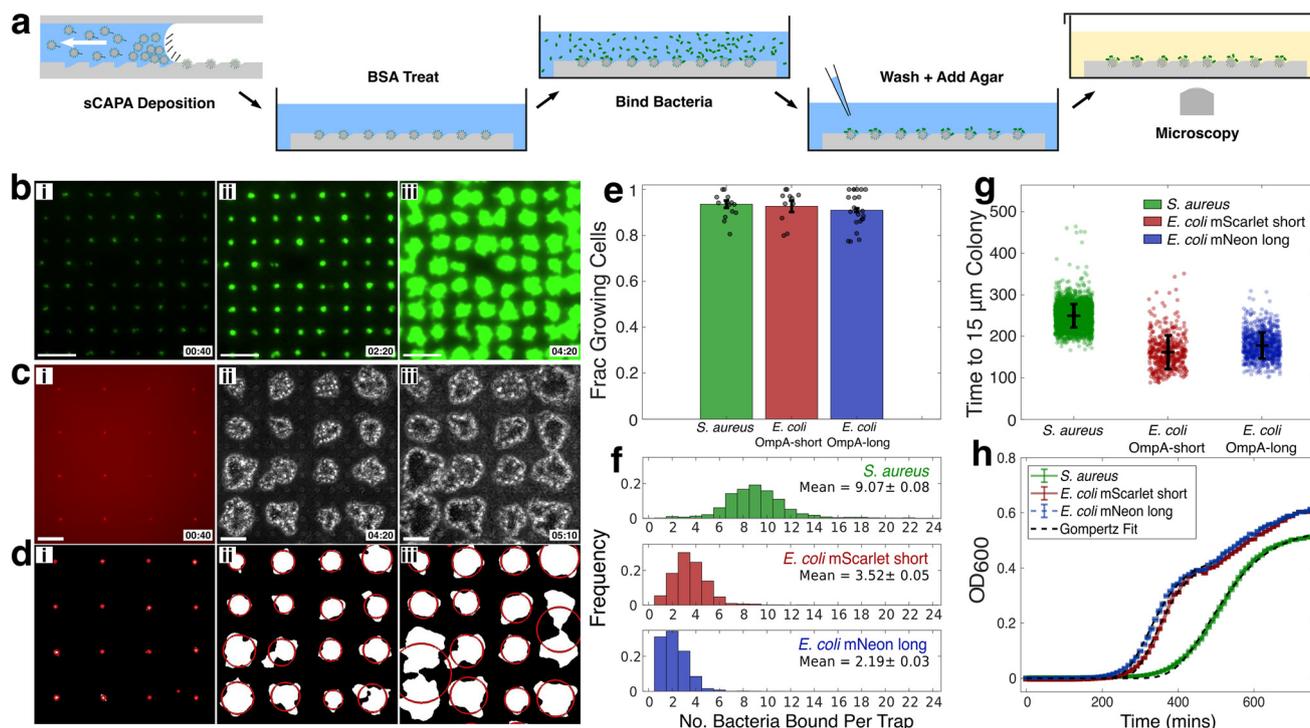
Fig. 4 Single species growth upon bacterial binding to sCAPA deposited particles. a) Graphical illustration of deposition and binding assay. Particles are first deposited with sCAPA, and the template is then transferred to a Petri dish and filled with BSA to cover the PDMS. Bacteria are then added to bind to the particles. Unbound bacteria are washed out with fresh PBS using a pipette. PBS is then replaced with agar media, before placing the petri dish under a microscope to image cell growth. b) Representative fluorescence images of *S. aureus* JE2 GFP bound to SbF1 deposited particles. i) Cells bound at $t = 40$ min after adding tryptone soy agar. ii) Cells growing after $t = 140$ min. iii) Cells growing at $t = 260$ min where colonies begin to merge. Scale bar = 50 μm. c) *E. coli* MC1061 mScarlet bound to Nb01 deposited particles. i) Cy3 image of cell binding at $t = 40$ min. ii) Phase contrast image of cell growth after $t = 260$ min. Cy3 fluorescence not visible at exponential phase due to weak fluorescence. iii) Cell growth at $t = 310$ min where colonies begin to merge. Scale bar = 50 μm. d) Binarised images in c used during image quantification. Binarised colony in white, red circles represent a circle with an equivalent area as overlaying colony to which a 'colony radius' is attributed. i) Cells bound at $t = 40$ min after adding tryptone soy agar, ii) colony formation after 260 min growth, iii) colonies begin to merge at 310 min. e) Quantification of the fraction of traps with observed microbial growth. Bars and errors represent mean and standard error of the mean, data points represent different fractions measured for each field of view for 3 separate templates for each bacterial strain. f) Distribution of number of bacteria bound in each trap as determined by particle localisation image analysis on ×60 magnification images of templates in PBS. Despite the particles all being the same size, the average number of bound bacteria to each particle notably varies. Mean number of bound bacteria and standard error of the mean displayed in top right. g) Distribution in time taken for individual colonies to reach a radius of 15 μm. Data points represent single growing colonies. Distributions represent all data for biological triplicates. Black lines represent mean and variance. h) Growth of indicated bacterial strains in liquid tryptone soy broth measured by optical density at 600 nm. Error bars represent standard error of the mean of 3 biological repeats and the black dotted line represents fit to a Gompertz growth law.

suspension for 10 minutes before repeatedly washing the template with fresh PBS. With this approach, we reliably bound bacteria to our particles with high species-selectivity and minimal non-specific binding to the PDMS surface.

To grow the initially bound cells into micro-colonies, we exchanged the PBS with molten tryptone soy broth agar kept at 50 °C and placed the well in the microscope for imaging. A detailed protocol on the agar exchange is provided in SI S5 together with a graphical outline of the full method. Fig. 4b and c and Movies S1 and S2 demonstrates targeted binding of *E. coli* and *S. aureus* and time-lapse imaging of colony growth after binding. Bacteria form into growing colonies that can be easily monitored from their initial particle-bound configuration. We found that single cells of *E. coli* mNeonGreen did not exhibit very strong fluorescence compared to the autofluorescence of the agar during growth at exponential phase. The fluorescence intensity of both *E.*

coli mNeonGreen and mScarlet changed during the growth phase with the average cell fluorescence decreasing as the cells entered exponential phase (SI S6). This weak fluorescence profile is due to a combination of promoter choice combined with our choice to express the fluorophore on the chromosome of the *E. coli* strains, rather than using high copy number plasmids for fluorophore expression (as in the case of *S. aureus*). We chromosomally integrated the fluorophore to avoid plasmid competition with the OmpA-long expression plasmid, but this had the downside that there was only one fluorescence gene in the cell. Despite this, we found that bacteria growth could be monitored in the brightfield or phase contrast channel thus fluorescent reporting during cell growth was not a critical requirement of the technique (Fig. 4c and d).

We quantified the growth dynamics and binding efficiency of cells in our method using an image analysis pipeline

designed to identify the location of deposited particles and track growing colonies (Fig. 4d–g). Importantly, colonies could only be tracked until the point where they merge with neighbouring colonies (Fig. 4b–d iii and SI S7 show representative colony merge events after which tracking colonies reliably is no longer viable). Thus, the maximum time frame over which bacteria growth can be analysed depends on the template design, specifically the distance between traps. In Fig. 4e, we find that for all bacterial strains tested, cells grew at almost all bound particles indicating that the protocol does not induce substantial stress or mortality on the cells. In Fig. 4f and SI S8, we observe large differences in the number of bacteria bound per particle, with the average number of bound *S. aureus* as high as 9.07 ± 0.08 cells per particle but *E. coli* binding at 3.52 ± 0.05 and 2.19 ± 0.03 for *E. coli* (OmpA-short) and *E. coli* (OmpA-long) respectively. This is in line with what was qualitatively observed in Fig. 3.

We measured the distribution in time taken for individual colonies to reach a radius of 15 μm in Fig. 4g and found a clear difference between *S. aureus* and *E. coli* with average lag-time and variance at 249 ± 28, 161 ± 41, 178 ± 32 minutes for *S. aureus*, *E. coli* mScarlet (OmpA-short) and *E. coli* mNeonGreen (OmpA-long), respectively. We benchmark these measurements from sCAPA against growth curve measurements in TSB media (Fig. 4h), which show strong agreement in lag-time data. By fitting a Gompertz growth law to these curves, we extract lag times and growth rates for all

cells (see SI S9 for details on fit), measuring 390 ± 4, 284 ± 4, 263 ± 3 minutes for *S. aureus*, *E. coli* mScarlet (OmpA-short) and *E. coli* mNeonGreen (OmpA-long), respectively. While the definition of lag time is not directly comparable to the time to reach a 15 μm radius colony, they show similar trends. We further observe that mScarlet *E. coli* strains have a slightly delayed lag time of ≈20 minutes compared to mNeonGreen strains, suggesting a small fitness disadvantage associated with the fluorophore expression (SI S9).

Controlling spatial structure between pairs of interacting bacteria

Bringing the protocol together, we combine the approaches developed above to assemble synthetic bacterial communities with high spatial specificity. In Fig. 5, we showcase targeted binding and growth of two species after sequential deposition of two particles (graphical illustration of method provided in SI S5). Fig. 5a and b and Movies S3 and S4 demonstrate binding and growth of *E. coli* mScarlet (OmpA-short) and *E. coli* mNeonGreen (OmpA-long) with spatial correlations corresponding to Moran's *I* values of −1 and 0.75, respectively. Fig. 5c and Movie S5 shows *S. aureus* GFP growing in a 1 : 24 ratio to *E. coli* (OmpA-long).

In order to perform sequential depositions, we had to include a heating step as previously noted. In order to determine how robust the nanobodies were to this heating step, we screened bacteria binding yield against repeated
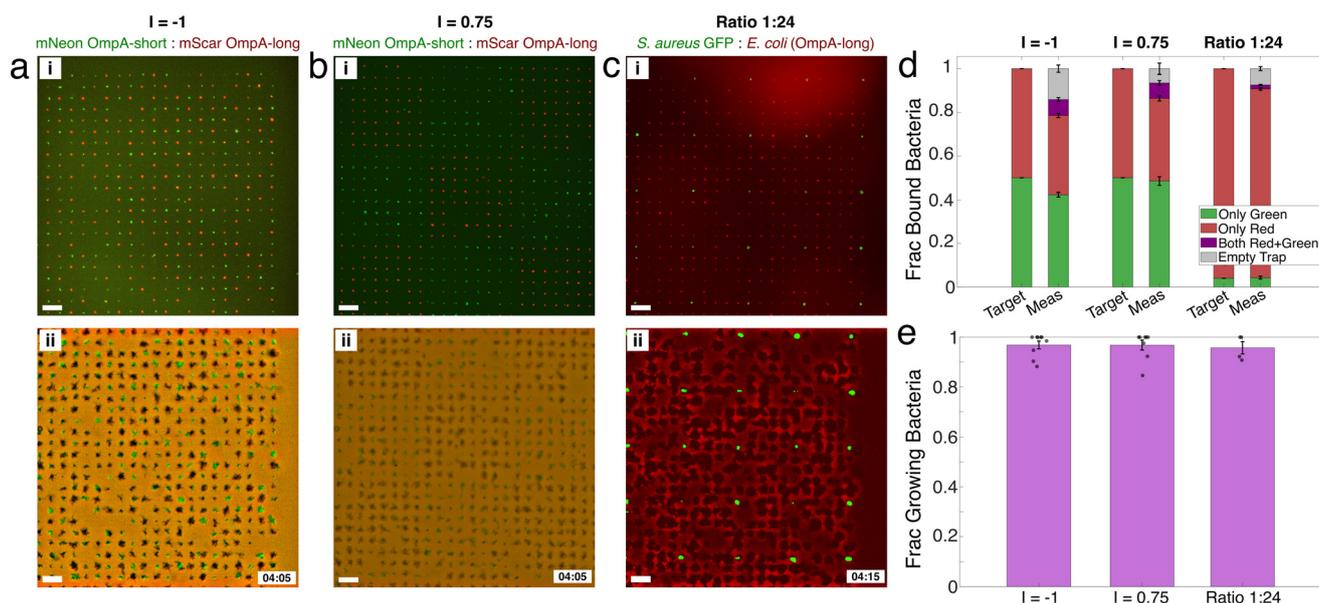

Fig. 5 Cell binding of microbial pairs with designed spatial structure. a–c) Representative images of selectively bound and growing cells across different time points. a) *E. coli* mScarlet (OmpA-short) and *E. coli* mNeonGreen (OmpA-long) in a sodium chloride lattice structure corresponding to Moran's *I* = −1. b) *E. coli* mScarlet (OmpA-short) and *E. coli* mNeonGreen (OmpA-long) in 8 × 8 patchy lattice structure corresponding to Moran's *I* = 0.75. c) *S. aureus* GFP and *E. coli* mScarlet (OmpA-long) in 1 : 24 ratio square lattice. i) Merged Cy3 and FITC image in PBS media, ii) cell growth after exchanging PBS with tryptone soy agar and growing at 37 °C. Distance between traps in all lattices is 25 μm. Time stamp in hours: mins after exchanging PBS for agar. Scale bar = 50 μm. d) Comparison of ideal *vs.* measured cell binding for spatial structures in a–c. Bars represent mean of 4 independent templates. e) Fraction of growing cells for sum of green and red cells. Data points represent measured growing fraction in individual microscope fields of view, for 4 independent templates. Error bars represent standard error of the mean.

heating steps of the template before binding (SI S10). We found that while the binding yield after 1 heating step was 93 ± 1%, it dropped to 50 ± 5% after 3 heating steps and <2% after 5 heat steps. We therefore found that an upper bound of 3 particle depositions was the highest, realistically achievable number of depositions using this approach to resolve the adhesion problem.

In Fig. 5d, we quantify the fraction of bound bacteria compared to target controls after 2 particle depositions and binding both bacteria species. We observed good agreement between the target configuration and the measured configuration. We measure that the fraction of empty traps is 0.14 ± 0.02, 0.06 ± 0.03, 0.07 ± 0.01 and that the fraction of traps with both green and red is 0.07 ± 0.01, 0.07 ± 0.01, 0.003 ± 0.01 for configurations a, b and c, respectively. These values are in good agreement with the deposition yields measured in Fig. 1e, indicating that imperfections in the target lattice derive primarily from imperfections in the particle deposition, rather than incomplete cell binding to the particles. Finally, in Fig. 5e, we measure a high fraction of total growing cells at each trap, demonstrating that both species grow and the cells are highly viable. Taken together, our data demonstrates that we can selectively deposit two bacteria species in well-defined spatial configurations, grow these cells and accurately quantify cell growth. We have, therefore, successfully developed a methodology that can be leveraged to investigate bacterial interactions with defined spatial structure.

Discussion

Methodological constraints in controlling the position of microbes with high precision has, to date, limited experimental investigation into how spatial structure and length scales shape microbial interactions. In this work, we have demonstrated a protocol for patterning and culturing two bacterial species with micron-scale precision, near single-cell resolution (2–9 bacteria bound per particle) and high throughput (we can pattern >10⁵ particles per template). The method can be performed in any standard microbiology laboratory and is simple to parallelise, allowing multiple biological repeats or spatial structures to be investigated in one experiment. Droplet 3D printing[27,30] and photolithographic-based printing[31] are, to date, the only two methods demonstrated to enable immobilisation and tracking of pairs of organisms in defined spatial structures, yet these approaches are typically labor-intensive and difficult to parallelise for many biological repeats. Our method contributes to this select group of protocols, while preserving both high throughput and high resolution in one technique.

A key feature of our method is the fact that the spatial patterning is decoupled from the bacteria binding. While previous work has demonstrated that bacteria can be directly patterned into traps using capillary assembly,[45,46] this is largely limited to patterning single organisms due to poor adhesion of the cells to the template, leading to cells being

removed from the traps after the second deposition and therefore preventing sequential depositions of different organisms.[54] It further requires a desiccation step, which has been shown to be problematic for certain organisms[45] as desiccation is a known cause of stress.[55,56] Our procedure resolves both these issues by depositing particles, instead of bacteria, and thus allows any cell to be bound in liquid culture followed by growth and imaging with minimal stress to the organism.

Our results also extend the versatility of sCAPA by demonstrating that particles of the same size can be patterned in wedge-shaped traps. While this in principle can be used to deposit up to 4 particles of the same size on one template, it can also be combined with different-sized traps that fit smaller or larger particles.[43,44] This approach, in principle, allows for the extension of this technique to much larger numbers of particle combinations. We note that changing the particle size, however, would impact the number of bacteria that bind per particle (Fig. 4e). By reducing the particle size (sCAPA is routinely performed with 1 μm particles[38,42]), the bacteria/particle ratio would move closer to 1 cell per particle, while increasing the particle size (sCAPA has been performed with particles up to 10 μm in diameter[57]) would increase this ratio.

A critical requirement for our approach is the access to selective binding moieties that can be used to selectively capture different bacterial species or strains. In principle, there is a wide range of binding moieties that can be used including antibodies, lectins, DNA aptamers, phage-tail proteins and others. While screening kits of antibodies and lectins can be bought from a range of vendors, these typically cannot achieve sufficient target specificity at the species level.[47] For this reason, we focused on nanobodies, which can be generated using nanobody libraries (as in this work)[58] and are small enough to access conserved regions on the cell membranes enabling high species-selectivity.[47,48] While not tested here, DNA aptamers may also be a promising approach as novel binding moieties can be rapidly generated via Cell-SELEX.[59]

To investigate the robustness of our method, we used nanobodies that bind to long and short forms of E. coli outer membrane protein (OmpA). We demonstrated that we could achieve fully selective cell patterning based solely on expression of 2 variants of the same protein. In order to demonstrate this, we designed an E. coli knockout mutant expressing OmpA-long on a high copy number plasmid. To avoid plasmid competition and plasmid loss within these cells, we therefore chromosomally integrated the fluorescent genes mScarlet and mNeonGreen into these cells which had the effect of lowering the maximum fluorescence of the strain compared to if we were to use a high copy number fluorescence plasmid. For this reason, the cell fluorescence of the E. coli strains was too weak to be visible during growth under the microscope (Fig. 4c and SI S6), unlike the case of S. aureus which expressed GFP on a high copy number plasmid. We found this not to be problematic for showcasing

our methodology as non-fluorescent colony growth can be easily tracked (Fig. 4d). Fluorescence was only required for identification of the initial location of bacteria at the start of the time-lapse. Nonetheless, we emphasise that the choice of nanobody, protein target and fluorescence expression approaches should be chosen wisely.

Finally, as mentioned above, the heating step required to improve particle adhesion during sequential depositions constitutes an important practical limitation to extending our protocol beyond 2–3 bacterial species. Furthermore, while previous work showed that biotin–streptavidin bound DNA[40,60] withstands a similar heating step, we cannot fully rule out the possibility of denaturation of larger proteins such as antibodies or lectins. In order to apply the technique developed here to larger numbers of species, therefore, alternative, *i.e.* chemical, strategies to improve particle adhesion after deposition need to be explored.

In conclusion, bacteria are social organisms that live in diverse, competitive and spatially structured communities. Fundamental questions regarding the limits of microbial coexistence and what determines the composition of microbial communities abound. We envisage the method presented here will help to better understand the role that length-scales and spatial structure play in shaping microbial interactions, starting from minimal models and paving the way towards more complex communities.

Materials and methods

Fabricating PDMS templates and microfluidic chips for sCAPA

sCAPA was performed in microfluidic chips made of polydimethylsiloxane (PDMS) consisting of a 'roof' designed to control the direction of the meniscus' motion and a ~0.4 mm 'template' containing the array of particle cavities, which we refer to as 'traps'. Chip design is illustrated in SI S1 and trap design is illustrated in Fig. 1. The negative molds for PDMS templates were designed using OpenSCAD and fabricated using a high-resolution 3D printer (Photonic Professional GT2, NanoScribe GmbH). All print file details are provided in the SI S11. Trap arrays were printed using commercial photo-resist (IP-dip, NanoScribe GmbH) onto fused silica glass slides (NanoScribe GmbH). After printing, the substrates were developed in propylene glycol methyl ether acetate (PGMEA) for 20 minutes, washed in isopropanol for 3 minutes and cured overnight under a UV lamp. Templates were then plasma-treated (Zepto Plasma Unit, Diener electronic GmbH) in air for 30 s and silanised with trichloro(1*H*,1*H*,2*H*,2*H*-perfluorooctyl)silane *via* vapour deposition to reduce adhesion to the mold such that cured PDMS would easily detach.

Molds for the chip roofs were designed as performed previously.[46] Briefly, a Prusa SL1 3D printer was used to print roof molds, which were washed in isopropanol solution, cured under UV overnight, left in the oven at 100 °C overnight to remove any non-cured resin and silanised as above.

Templates and chip roofs were prepared using polydimethylsiloxane (PDMS; Sylgard 184 silicone elastomer kit, Dow Corning, Midland, MI). PDMS was mixed and degassed in a 10:1 ratio of polymer:crosslinker using a Thinky ARE-250. For the chip roofs, 20 g of PDMS was poured onto the 3D printed mold, wrapped with aluminium to form a box around the mold. For the template, printed slides were placed in a 60 mm plastic Petri dish, and 2 g of PDMS was poured over such that a uniform layer of thin PDMS covered the whole area of the glass and the bottom of the Petri dish. After curing overnight at 75 °C, PDMS was cut out using a scalpel and 1 mm diameter holes were punched into the PDMS roofs. The PDMS chips were assembled by bonding the roofs to the templates using microscope spacers (Grace Bio-Labs SecureSeal), which were designed on a cutting plotter (Silhouette Cameo 4). This process made it simple to remove the roofs from the templates after deposition.

Streptavidin functionalisation of silica particles

Silica particles were functionalised with streptavidin according to a previously reported method,[41] adapted originally from ref. 61. 0.5 ml 5 w/v% particles were washed 3× with Milli-Q water. The particles were then cleaned by adding 0.5 ml 30 w/w% hydrogen peroxide (Sigma-Aldrich) and 0.5 ml 25 w/w% ammonia (Sigma-Aldrich) together in a round-bottom flask and heating to 70 °C in an oil bath for 10 minutes in order to remove any impurities and activate the silica surface. The particles were then washed 3× with 1 ml Milli-Q water and 3× with 1.5 ml ethanol (>98.8% purity) before adding 70 μl APTES (ACROS, 99%), and gently mixing for 16 hours. APTES-modified particles were then washed 3× with ethanol as before and 3× with 1 ml phosphate-buffered saline (PBS). Particles were resuspended in 1 ml PBS and 0.1 w/w% Pluronic F127 before adding 1 ml 25 v/v% glutaraldehyde to 0.5 ml particle suspension and mixed in a rotary stirrer for 3 hours. Glutaraldehyde-modified particles were then cleaned 5× with 1 ml PBS and 0.1 w/w% Pluronic F127. 100 μl of 2 mg ml^{-1} streptavidin (Apollo Scientific, 97%) in PBS was then added and left for 16 hours under gentle stirring for the reaction to proceed. The streptavidinated particles were finally washed 3× with 50 mM phosphate + 50 mM NaCl and suspended in 1 ml of storage buffer (50 mM phosphate, 50 mM NaCl and 0.001 w/w% NaN$_3$). The final concentration was ~2.5 w/w% and stored in the fridge at 4°.

Fluorescent biotin functionalisation of streptavidin particles

2.7 μm streptavidin-functionalised silica particles were made fluorescent by adding 1 μl 0.2 mM Atto-550 or Atto-488 fluorescent biotin (Sigma Aldrich) to 200 μl 0.25 wt% silica particles suspended in 50 mM Tris-HCL buffer (pH 9.0). The mixture was left for 30 min in a benchtop orbital to rotate before washing 3× with 50 mM Tris-HCL buffer. The final 0.25 wt% fluorescent particle suspension was stored in the refrigerator until use.

Sequential particle depositions with sCAPA

Particle arrays were constructed by sequential depositions into directional, wedge-shaped traps. All particle depositions were performed using 0.08 wt% silica particles (functionalised with either Alexa Fluor-biotin or nanobodies – see below) suspended in 50 mM Tris-HCL buffer with 0.1 v/v% Tween20. PDMS chips were arranged on glass slides to make it easy to move chips around, 30 µl of a particle suspension was then placed in each PDMS chip using a pipette and the chip was left on a heat plate (IKA RCT Basic Hot Plate Stirrer) at 35 °C for approximately 1 hour or until the deposition was finished. After the particle deposition, the PDMS roof was removed and the template was placed on a heat plate set to 130 °C for 1 minute (equivalent to 87 ± 1 °C on the PDMS surface). This step was necessary to promote adhesion of the particles to the traps, otherwise any further depositions or bacteria binding steps could lead to detachment of the deposited particles (see Results, SI S3 for details on temperature measurements, SI S10 for affect of repeated heat cycles on nanobodies). Any subsequent depositions were performed by placing a new, clean roof on the template and repeating the deposition as above in the opposite direction.

Bacteria strains and growth protocol

The *S. aureus* USA300 JE2 strain expressing GFP was constructed by transforming USA300 JE2 with a pCN56 plasmid containing the *gfp* gene under the control of the BlaZ promoter (Zinkernagel lab). For *E. coli*, we developed chromosomally fluorescent strains expressing mNeonGreen or mScarlet proteins in *E. coli* MC1061 (ATCC 37493, obtained from the lab of Markus Seeger). This was performed in both a wild type strain and in an outer membrane protein A (OmpA) knockout strain. As wild type MC1061 natively expresses the short form of OmpA, this strain we refer to as '*E. coli* (OmpA-short)'. To develop the '*E. coli* (OmpA-long)' strain, we expressed the long form of OmpA, under control of the pBAD promoter, on a pBXNPH3 plasmid in the fluorescent OmpA-short knockout strains. A list of all strains used in this study and details on the construction of strains are detailed in the SI S12.

All overnight cultures for binding assays were grown by the following: frozen stocks kept at −80 °C were plated on agar plates containing either lysogeny broth (LB) agar, LB agar + 100 µg ml⁻¹ ampicillin or tryptone soy broth (TSB) agar + 10 µg ml⁻¹ erythromycin for *E. coli* (OmpA-short), *E. coli* (OmpA-long) and *S. aureus*, respectively. Liquid cultures were prepared by inoculating single colonies from plates in 50 ml falcon tubes containing 5 ml TSB and either no antibiotic, 100 µg ml⁻¹ ampicillin or 10 µg ml⁻¹ erythromycin for *E. coli* (OmpA-short), *E. coli* (OmpA-long) and *S. aureus*, respectively. Cultures were placed in an incubator (Edmund Buehler TH30 Incubation Hood), with lids loosely closed, at 37 °C with orbital shaking at 220 rpm and grown overnight. 1 hour before beginning an experiment, we added 0.02 wt/v% L-arabinose to the *E. coli* (OmpA-long) cultures to induce OmpA-long expression.

OD growth curves

To normalise cell concentrations at the start of OD growth curves, the absolute cell numbers at a given OD_{600} of *S. aureus* and *E. coli* strains was determined by serial dilutions of overnight cultures, plating on agar overnight and quantifying colony formation units (cfu). Overnight cultures of various strains were then diluted to a final concentration of 10^5 cfu ml⁻¹ in TSB media containing the appropriate antibiotics in a clear, flat bottom 96-well plate with a final volume of medium at 200 µL. The plate was then sealed with parafilm, moved to a Synergy H1 microplate reader (BioTek) and grown for 48 h at 37 °C with kinetic settings of 10 min cycles, shaking for 10 s prior to each measurement. Resulting growth curves were plotted using Matlab and zeroed using the formula: $OD_{reported} = OD_{t_i} - OD_{t_0}$.

Nanobody generation

Three nanobodies, Nb01, Nb41 and SbF1, were used in this study to selectively bind to the cell surface of *E. coli* (OmpA-short), *E. coli* (OmpA-long) and *S. aureus* respectively (sequences provided in SI S12). Generation and characterization of Nb01 has been described previously.[48] Nb41 was also described in the same article, however this was not one of the main nanobodies characterised for *E. coli* (OmpA-long). Nb41 was selected because it does not bind protein A (due to amino acid differences in the Fc-like domain), and hence does not cross-react with *S. aureus*. The *S. aureus* targeting synthetic nanobody SbF1, was generated *via* screening of a synthetic nanobody (sybody) library[58,62] against biotinylated protein A. Protein A (P3838, Sigma) was biotinylated by adding 10-fold molar excess of NHS-biotin (EZ-Link™ NHS-Biotin, Thermo Scientific) and incubating at room temperature for 45 minutes.[63] Excess NHS-Biotin was removed using a PD MidiTrap G-25 (28918008, Cytiva) desalting column equilibrated with degassed PBS, pH 7.4. Screening of the synthetic library started with synthetic nanobodies displayed on ribosomes for pre-enrichment, followed by two rounds of phage display and binder identification by ELISA as described in the protocol by Zimmermann *et al.*[58] All sybodies have an Fc-like side domain which binds to protein A.[52] Hence, we performed a sandwich ELISA to screen for binders that additionally bind *via* CDRs for tighter binding, thereby identifying SbF1.

For orthogonal labelling, the three nanobodies were cloned into the pSBinit_cys plasmid where a cysteine residue is incorporated at the C-terminus of the nanobody.[48] The nanobodies were expressed in *E. coli* MC1061 Δ*ompA* (for Nb01) or *E. coli* MC1061 (for Nb41 and SbF1) as described in ref. 58. Following periplasmic extraction, supernatants were subjected to Ni-NTA affinity chromatography (Qiagen) and Size Exclusion Chromatography (SRT SEC-100 or SRT SEC-300, Sepax) using PBS as running buffer.

To attach the PEG linker (PEG11-Biotin, Catalog # 21911, ThermoFisher) using maleimide chemistry, the free thiol group needs to be protected from oxidation before exposure

to the linker. Therefore, purification of these cysteine-containing nanobodies was performed in the presence of 2 mM DTT. After nanobody purification, DTT was removed using a PD MidiTrap G-25 desalting column equilibrated with degassed PBS, pH 7.0. Maleimide functionalised PEG11-Biotin, was added at 3.6-fold molar excess and the reaction was carried out for 1 h at 4 °C. Excess label was removed using another PD MidiTrap G-25 column, equilibrated with PBS, pH 7.4. Stock concentrations of 300.8 μM NB01, 62.1 μM SbF1 or 15.6 μM NB41 were aliquoted and stored at −20 °C.

Conjugating nanobodies to streptavidin particles

To conjugate nanobody–PEG11 molecules to particles, 100 μl of 0.25 w/w% streptavidin functionalised silica particles were washed 3× in 1 ml 50 mM Tris-HCl buffer (Trizma base, Sigma-Aldrich), pH 9.0. 20 μl of this suspension was added to 175 μl Tris-buffer in a 1.5 ml Eppendorf tube and 5 μl 2 v/v% Tween 20 was added to lower the surface tension and aid mixing. Aliquots of nanobody–PEG11 conjugates were then defrosted and added to the particle suspension to a final concentration of 0.75 μM. Nanobody-particle suspensions were then left to conjugate to the particles for at least 2 hours in a bench-top orbital rotator before gently centrifuging and replacing the supernatant with 0.2 mg ml^{-1} biotin in 50 mM Tris buffer and 0.05 w/v% Tween 20 to block any non-bound streptavidin sites. Particles were then gently resuspended and left in the orbital rotator for 10 minutes. Finally, particle suspensions were gently washed 3× with 50 mM Tris buffer and stored in the fridge at 4 °C.

Control particle–bacteria binding assay in bulk

Control binding in Fig. 3 was performed by mixing nanobody-functionalised particles with bacteria in a 1.5 ml Eppendorf in an orbital rotator. 5 μl 0.025% nanobody functionalised particles were placed in 170 μl PBS, 5 μl 2 v/v% Tween 20 and 20 μl overnight bacterial culture that had been washed 3× in PBS. Tween 20 was added to lower the surface tension and aid mixing. Particle–bacteria mixtures were placed in an orbital rotator for 30 min before being gently pipetted into a 96-well plate and imaged with a Nikon Eclipse TI2-E inverted microscope to check binding.

Bacteria binding and growth after sCAPA deposition

After completing sequential particle depositions, templates were placed in a 25 mm glass-bottom μ-Dish (Ibidi). The dish was filled with 2 ml 2% bovine serum albumin (BSA, Sigma-Aldrich) in PBS and left in the incubator for 10 minutes in order to passivate the PDMS surface. Overnight cultures of bacteria were washed 3× in pre-warmed PBS before replacing the BSA solution with 2 ml of cell suspension. The dish was then sealed with parafilm and left in an orbital rotator to gently mix at 80 rpm for 15 minutes. After binding, the template was washed up to 8× with fresh, pre-warmed PBS taking significant care not to remove so much liquid as to

allow the PDMS to dewet (*i.e.* dry the template). If binding a second bacterium, the washed overnight culture was then added and placed back in the orbital shaker for 15 minutes before washing again. After sufficient washing in PBS, pre-melted tryptone soy agar (1.5 wt% agar, Sigma Aldrich) kept in a heat bath at 50 °C was gently poured into the dish from a falcon tube while removing the PBS at the other end using a pipette. This allowed us to gently exchange the PBS with TSA. Once the TSA had gelled, the dish was sealed with parafilm and placed in a Nikon Eclipse TI2-E inverted microscope pre-warmed at 37 °C for imaging and growth. All time-lapse imaging was performed using the Nikon NIS elements software. We used the *XY* overview panel to define areas on each template to ensure no images overlapped during acquisition.

Image analysis

A custom MATLAB script was written to perform the image analysis, previously detailed in ref. 46. The analysis pipeline is summarised here.

Background correction of images was first performed on ImageJ before importing images onto MATLAB. For the fluorescence channel, all frames in the time-lapse were divided by a strongly Gaussian-blurred image (sigma = 200 pixels) of the first frame in the time-lapse. As the relative brightness in the brightfield channel changed substantially throughout the time-lapse, background normalisation of the brightfield channel was performed by dividing each frame in the time-lapse by a strongly Gaussian blurred (sigma = 200 pixels) version of the same frame. Particle localisation was performed using the MATLAB version[64] of the Crocker and Grier algorithm[65] on the first frame in the time-lapse, to identify the centroid of all fluorescent cells (when performed in the fluorescence channel) and the location of particles (when performed on the brightfield channel). A minimum brightness thresholds to identify a particle was set as 3× the average brightness noise in the image and the length scales of objects identified in the image (used in the band pass filter to select objects based on size), were set to: length scale of salt and pepper noise = 1 pixel (0.32 μm), length scale of bacteria set to 3 pixels (0.98 μm), length scale of particle per trap set to 15 pixels (4.88 μm).

To identify growing bacteria, all background-subtracted images in the time-lapse were binarised using a fixed brightness threshold. For non-fluorescent tracking, *i.e. E. coli* growth, we inverted the brightfield channel such that growing colonies appeared bright on a dark background before thresholding. The area of the identified growing colonies was determined at each time point allowing the colony area and radius (calculated as $\sqrt{\frac{A_{\text{colony}}}{\pi}}$ to accommodate non-circular colonies) to be extracted.

We linked colonies across time frames *via* the following procedure: firstly, an image registration step was performed against the first frame in the time-lapse, in order to account

for spatial drift during the time-lapse. This ensured all identified bacteria positions were in the same coordinate system. To do this, we performed intensity-based image registration on a representative area in the brightfield channel that could easily be tracked throughout the entire time-lapse despite growth *e.g.* the corner of the template. For the time update, all colony centroids and radii were identified in frame t_i and t_{i+1} and a colony track was updated if a colony in t_{i+1} overlapped with another colony in t_i. If no colonies in t_i overlapped with one in t_{i+1}, a new cell was considered to have begun to grow, so a new colony was defined. If two colonies in t_i overlapped in t_{i+1}, the colonies were considered to have merged (*e.g.* SI S7). In this case, the tracking update was attributed to the larger of the two colonies, and the small colony was no longer updated. In practice, however, at the point where colonies start merging, the tracking is no longer reliable as the colony area of the larger colony jumps substantially.

Once colonies have been linked through time into tracks, a clean up step was performed. An identified growing colony was used in the analysis (*i.e.* considered to be a true growing colony) only if it fulfilled certain criteria: 1) the colony radius increases with time, 2) the colony is tracked for at least 5 consecutive frames, 3) the colony does not grow out of the field of view (whereupon the colony area would not be correctly determined), 4) the colony grows to a radius of at least 15 μm. For colonies that fulfill these criteria, the colony lag-time was defined as the time point when the colony diameter is >30 μm. As a consequence of these strict criteria, the analysis code may slightly underestimate the number of growing colonies in the time-lapse.

Author contributions

Author contributions are defined based on the CRediT (Contributor Roles Taxonomy) and listed alphabetically. Conceptualisation: C. B., E. S., L. I.; data curation: C. B., J. P. H. W., A. S.; formal analysis: C. B.; funding acquisition: L. I., M. S., A. S. Z.; investigation: C. B., J. P. H. W.; methodology: C. B., J. P. H. W.; project administration: C. B., L. I.; resources: C. B., A. S., M. S.; software: C. B.; supervision: A. S. Z., M. S., E. S., L. I.; validation: C. B.; visualisation: C. B., E. S., L. I.; writing – original draft: C. B., J. P. H. W., E. S., L. I.; writing – review and editing: C. B., J. P. H. W., A. S., M. S., E. S., L. I.

Conflicts of interest

The authors declare that they have no competing interests.

Data availability

All code and processed image data used to generate figures are available on the ETH Zurich Research Collection, accessible *via* https://doi.org/10.3929/ethz-c-000794495. Due to the very large file size (several TBs), raw image data will not be uploaded but will be provided on request.

Supplementary information (SI) is available. See DOI: https://doi.org/10.1039/d6lc00040a.

Notes and references

1 J. D. Palmer and K. R. Foster, *Science*, 2022, **376**, 581–582.
2 B. L. Hardy and D. S. Merrell, *J. Bacteriol.*, 2021, **203**, 10–1128.
3 O. S. Venturelli, A. V. Carr, G. Fisher, R. H. Hsu, R. Lau, B. P. Bowen, S. Hromada, T. Northen and A. P. Arkin, *Mol. Syst. Biol.*, 2018, **14**, e8157.
4 M. Ghoul and S. Mitri, *Trends Microbiol.*, 2016, **24**, 833–845.
5 C. D. Nadell, K. Drescher and K. R. Foster, *Nat. Rev. Microbiol.*, 2016, **14**, 589–600.
6 S. A. West, A. S. Griffin, A. Gardner and S. P. Diggle, *Nat. Rev. Microbiol.*, 2006, **4**, 597–607.
7 J. Dolinšek, F. Goldschmidt and D. R. Johnson, *FEMS Microbiol. Rev.*, 2016, **40**, 961–979.
8 M. Whiteley, S. P. Diggle and E. P. Greenberg, *Nature*, 2017, **551**, 313–320.
9 B. Kerr, M. A. Riley, M. W. Feldman and B. J. Bohannan, *Nature*, 2002, **418**, 171–174.
10 H. J. Kim, J. Q. Boedicker, J. W. Choi and R. F. Ismagilov, *Proc. Natl. Acad. Sci. U. S. A.*, 2008, **105**, 18188–18193.
11 K. Z. Coyte, J. Schluter and K. R. Foster, *Science*, 2015, **350**, 663–666.
12 K. Drescher, C. D. Nadell, H. A. Stone, N. S. Wingreen and B. L. Bassler, *Curr. Biol.*, 2014, **24**, 50–55.
13 A. Conwill, A. C. Kuan, R. Damerla, A. J. Poret, J. S. Baker, A. D. Tripp, E. J. Alm and T. D. Lieberman, *Cell Host Microbe*, 2022, **30**, 171–182.
14 S. A. Wilbert, J. L. M. Welch and G. G. Borisy, *Cell Rep.*, 2020, **30**, 4003–4015.
15 J. L. Mark Welch, B. J. Rossetti, C. W. Rieken, F. E. Dewhirst and G. G. Borisy, *Proc. Natl. Acad. Sci. U. S. A.*, 2016, **113**, E791–E800.
16 D. Kim, J. P. Barraza, R. A. Arthur, A. Hara, K. Lewis, Y. Liu, E. L. Scisci, E. Hajishengallis, M. Whiteley and H. Koo, *Proc. Natl. Acad. Sci. U. S. A.*, 2020, **117**, 12375–12386.
17 C. Tropini, K. A. Earle, K. C. Huang and J. L. Sonnenburg, *Cell Host Microbe*, 2017, **21**, 433–442.
18 J. L. Mark Welch, Y. Hasegawa, N. P. McNulty, J. I. Gordon and G. G. Borisy, *Proc. Natl. Acad. Sci. U. S. A.*, 2017, **114**, E9105–E9114.
19 K. A. Earle, G. Billings, M. Sigal, J. S. Lichtman, G. C. Hansson, J. E. Elias, M. R. Amieva, K. C. Huang and J. L. Sonnenburg, *Cell Host Microbe*, 2015, **18**, 478–488.

20 V. B. Rudkjøbing, T. R. Thomsen, M. Alhede, K. N. Kragh, P. H. Nielsen, U. R. Johansen, M. Givskov, N. Høiby and T. Bjarnsholt, *FEMS Immunol. Med. Microbiol.*, 2012, **65**, 236–244.

21 M. Fazli, T. Bjarnsholt, K. Kirketerp-Møller, B. Jørgensen, A. S. Andersen, K. A. Krogfelt, M. Givskov and T. Tolker-Nielsen, *J. Clin. Microbiol.*, 2009, **47**, 4084–4089.

22 K. Kirketerp-Møller, P. Ø. Jensen, M. Fazli, K. G. Madsen, J. Pedersen, C. Moser, T. Tolker-Nielsen, N. Høiby, M. Givskov and T. Bjarnsholt, *J. Clin. Microbiol.*, 2008, **46**, 2717–2722.

23 R. J. van Tatenhove-Pel, D. H. de Groot, A. S. Bisseswar, B. Teusink and H. Bachmann, *ISME J.*, 2021, **15**, 3050–3061.

24 J. Kehe, A. Kulesa, A. Ortiz, C. M. Ackerman, S. G. Thakku, D. Sellers, S. Kuehn, J. Gore, J. Friedman and P. C. Blainey, *Proc. Natl. Acad. Sci. U. S. A.*, 2019, **116**, 12804–12809.

25 E. Osmekhina, C. Jonkergouw, G. Schmidt, F. Jahangiri, V. Jokinen, S. Franssila and M. B. Linder, *Commun. Biol.*, 2018, **1**, 97.

26 J. Baer, S. G. Charlton, A. Tarnutzer, G. S. Ugolini, E. Secchi and A. S. Zinkernagel, *bioRxiv*, 2024, preprint, DOI: 10.1101/2024.02.27.582246.

27 R. Krishna Kumar and K. R. Foster, *Microb. Biotechnol.*, 2023, **16**(3), 489–493.

28 T. G. Johnston, S.-F. Yuan, J. M. Wagner, X. Yi, A. Saha, P. Smith, A. Nelson and H. S. Alper, *Nat. Commun.*, 2020, **11**, 563.

29 A. K. Wessel, L. Hmelo, M. R. Parsek and M. Whiteley, *Nat. Rev. Microbiol.*, 2013, **11**, 337–348.

30 R. Krishna Kumar, T. A. Meiller-Legrand, A. Alcinesio, D. Gonzalez, D. A. Mavridou, O. J. Meacock, W. P. Smith, L. Zhou, W. Kim and G. S. Pulcu, *et al.*, *Nat. Commun.*, 2021, **12**, 857.

31 J. L. Connell, E. T. Ritschdorff, M. Whiteley and J. B. Shear, *Proc. Natl. Acad. Sci. U. S. A.*, 2013, **110**, 18380–18385.

32 R. Schmidt, D. Ulanova, L. Y. Wick, H. B. Bode and P. Garbeva, *ISME J.*, 2019, **13**, 2656–2663.

33 J. I. Prosser, *FEMS Microbiol. Ecol.*, 2012, **81**, 507–519.

34 A. Dal Co, S. van Vliet, D. J. Kiviet, S. Schlegel and M. Ackermann, *Nat. Ecol. Evol.*, 2020, **4**, 366–375.

35 A. Dal Co, S. van Vliet and M. Ackermann, *Philos. Trans. R. Soc., B*, 2019, **374**, 20190080.

36 R. J. van Tatenhove-Pel, T. Rijavec, A. Lapanje, I. van Swam, E. Zwering, J. A. Hernandez-Valdes, O. P. Kuipers, C. Picioreanu, B. Teusink and H. Bachmann, *ISME J.*, 2021, **15**, 688–701.

37 S. Gantner, M. Schmid, C. Dürr, R. Schuhegger, A. Steidle, P. Hutzler, C. Langebartels, L. Eberl, A. Hartmann and F. B. Dazzo, *FEMS Microbiol. Ecol.*, 2006, **56**, 188–194.

38 S. Ni, L. Isa and H. Wolf, *Soft Matter*, 2018, **14**, 2978–2995.

39 S. Ni, E. Marini, I. Buttinoni, H. Wolf and L. Isa, *Soft Matter*, 2017, **13**, 4252–4259.

40 S. van Kesteren, P. Diethelm, S.-H. Jung and L. Isa, *Small*, 2024, **20**, 2400180.

41 S. van Kesteren, L. Alvarez, S. Arrese-Igor, A. Alegria and L. Isa, *Proc. Natl. Acad. Sci. U. S. A.*, 2023, **120**, e2213481120.

42 S. Ni, J. Leemann, H. Wolf and L. Isa, *Faraday Discuss.*, 2015, **181**, 225–242.

43 S. van Kesteren, X. Shen, M. Aldeghi and L. Isa, *Adv. Mater.*, 2023, **35**, 2207101.

44 C. Kuemin, K. Cathrein Huckstadt, E. Lörtscher, A. Rey, A. Decker, N. D. Spencer and H. Wolf, *Adv. Mater.*, 2010, **22**, 25.

45 R. Pioli, R. Stocker, L. Isa and E. Secchi, *J. Visualized Exp.*, 2021, e63131.

46 C. Boggon, S. M. Shambat, A. S. Zinkernagel, E. Secchi and L. Isa, *Lab Chip*, 2023, **23**, 5018–5028.

47 M. Sorgenfrei, L. M. Hürlimann, M. M. Remy, P. M. Keller and M. A. Seeger, *Trends Biochem. Sci.*, 2022, **47**, 673–688.

48 M. Sorgenfrei, L. M. Hürlimann, A. Printz, F. Wegner, D. Morger, F. Ackle, M. M. Remy, G. Montowski, H. A. Keserue, A. Cuénod, F. Imkamp, A. Eglil and M. A. Seeger, *Commun. Biol.*, 2025, 1047.

49 M. Sorgenfrei, *PhD thesis*, University of Zurich, 2024.

50 M. L. Power, B. C. Ferrari, J. Littlefield-Wyer, D. M. Gordon, M. B. Slade and D. A. Veal, *Appl. Environ. Microbiol.*, 2006, **72**, 7930–7932.

51 C. Stathopoulos, *Protein Sci.*, 1996, **5**, 170–173.

52 P. C. Fridy, M. K. Thompson, N. E. Ketaren and M. P. Rout, *Anal. Biochem.*, 2015, **477**, 92–94.

53 M. Crauwels, N. Van Vaerenbergh, N. B. Kulaya, C. Vincke, M. D'Huyvetter, N. Devoogdt, S. Muyldermans and C. Xavier, *New Biotechnol.*, 2020, **57**, 20–28.

54 C. Boggon, *PhD thesis*, ETH Zurich, 2024, DOI: 10.3929/ethz-b-000706819.

55 J. Esbelin, T. Santos and M. Hébraud, *Food Microbiol.*, 2018, **69**, 82–88.

56 M. Potts, *Microbiol. Rev.*, 1994, **58**, 755–805.

57 Z. C. Meijs, H. S. Yun, C. Sirvinski, D. K. Yoon and L. Isa, *Liq. Cryst.*, 2024, **51**, 2426–2434.

58 I. Zimmermann, P. Egloff, C. A. Hutter, B. T. Kuhn, P. Bräuer, S. Newstead, R. J. Dawson, E. R. Geertsma and M. A. Seeger, *Nat. Protoc.*, 2020, **15**, 1707–1741.

59 K. Sefah, D. Shangguan, X. Xiong, M. B. O'donoghue and W. Tan, *Nat. Protoc.*, 2010, **5**, 1169–1185.

60 S. van Kesteren, P. Diethelm and L. Isa, *Soft Matter*, 2024, **20**(13), 2881–2886.

61 C. Hou, L. Zhang, Y. Wang and Z. Wang, *J. Appl. Polym. Sci.*, 2015, **132**, 9.

62 I. Zimmermann, P. Egloff, C. A. Hutter, F. M. Arnold, P. Stohler, N. Bocquet, M. N. Hug, S. Huber, M. Siegrist and L. Hetemann, *et al.*, *eLife*, 2018, **7**, e34317.

63 B. T. Kuhn, I. Zimmermann, P. Egloff, L. M. Hürlimann, C. A. Hutter, C. Miscenic, R. J. Dawson, M. A. Seeger and E. R. Geertsma, *Expression, Purification, and Structural Biology of Membrane Proteins*, 2020, pp. 151–165.

64 The Matlab Particle Tracking Code Repository, https://site.physics.georgetown.edu/matlab/, Accessed: 2025-12-30.

65 J. C. Crocker and D. G. Grier, *J. Colloid Interface Sci.*, 1996, **179**, 298–310.